Journal of Materials Chemistry A

RSC Publishing

PAPER

View Article Online
View Journal | View Issue

Cite this: *J. Mater. Chem. A*, 2013, **1**, 8209

Bicrystalline TiO_2 with controllable anatase–brookite phase content for enhanced CO_2 photoreduction to fuels†

Huilei Zhao,[a] Lianjun Liu,[a] Jean M. Andino[bc] and Ying Li*[a]

Received 26th March 2013
Accepted 25th May 2013

DOI: 10.1039/c3ta11226h

www.rsc.org/MaterialsA

Among the three naturally existing phases of TiO_2, brookite is the least studied as a photocatalyst. In this study, single-phase anatase and brookite, and mixed-phase anatase–brookite TiO_2 nanomaterials were synthesized through a hydrothermal method. The anatase–brookite phase content was controlled by adjusting the concentration of urea in the precursor solution. XRD, Raman spectroscopy, and high-resolution TEM were used to confirm the crystal structures. SEM and TEM analyses demonstrated that anatase TiO_2 were nearly spherical nanoparticles while brookite TiO_2 were rod-shaped nanoparticles. UV-vis diffuse reflectance spectroscopy showed a blue shift in absorption spectra with increasing brookite content. The photocatalytic activities of the prepared bicrystalline TiO_2 were evaluated for CO_2 photoreduction in the presence of water vapor for production of solar fuels (CO and CH_4). The activities were compared with those of pure anatase, pure brookite, and a commercial anatase–rutile TiO_2 (P25). The results showed that bicrystalline anatase–brookite was generally more active than single-phase anatase, brookite, and P25. The bicrystalline mixture with a composition of 75% anatase and 25% brookite showed the highest photocatalytic activity, likely due to the enhanced interfacial charge transfer between anatase and brookite nanocrystals. *In situ* DRIFTS analysis showed that CO_2^- and HCO_3^- species were active reaction intermediates for CO_2 photoreduction while the accumulation of non-reactive CO_3^{2-} species on the TiO_2 surface may be detrimental.

1 Introduction

The conversion of solar energy into fuels using CO_2 as the feedstock by photocatalysts such as TiO_2 offers significant promise in the development of a sustainable energy technology. The general products from CO_2 photoreduction by TiO_2 photocatalysts are CO, CH_4, CH_3OH, HCOOH, *etc.*[1–4] However, the well-known large band gap of TiO_2 and the fast recombination rate of the photogenerated electrons (e^-) and holes (h^+) have limited the development of solar fuel technology. Modifications of TiO_2 by metal deposition or non-metal doping have been attempted to improve the CO_2 conversion efficiency.[1,5]

Anatase, brookite, and rutile are naturally existing TiO_2 polymorphs.[6–9] Anatase based catalysts have been demonstrated to be highly active, while rutile is less active,[10,11] mainly due to the fast e^- and h^+ recombination in rutile.[12] Mixtures of anatase–rutile such as commercially available TiO_2 nanopowder, Evonik P25 (approximately 75% anatase and 25% rutile) have demonstrated higher photocatalytic activity than single-phase anatase or rutile crystals in various photocatalytic applications.[13,14] Brookite is rarely studied in photocatalysis likely due to the past difficulties in synthesizing high purity brookite because of its metastable property.[15–18] A few studies demonstrated the high activity of brookite in photocatalytic oxidation applications.[19,20] Our recent study[4] was the first one to investigate the activity of pure brookite TiO_2 for CO_2 photoreduction with water; brookite showed higher activity than rutile, and surface-defective brookite was even more active than anatase.

Mixed-phase TiO_2 nanomaterials other than commercial P25 TiO_2 nanoparticles are scarcely studied in CO_2 photoreduction, and the interactions of the different phases during the CO_2 photoreduction reactions have not been explored. It is believed that the junctions between different phases of TiO_2 play a significant role in improving its photo-oxidation activity.[6,7] Several studies have explored the mechanism for the enhanced activity of anatase and rutile mixtures such as P25; however, the findings are not conclusive. Some studies suggested that photoinduced electrons tend to transfer from the higher-level anatase conduction band (CB) to the lower-level rutile CB,[21] while the holes in the anatase valance band (VB) could migrate to the rutile VB.[11] On the

[a]*Mechanical Engineering Department, University of Wisconsin-Milwaukee, 3200 N Cramer St, Milwaukee, Wisconsin, USA. E-mail: liying@uwm.edu; Fax: +1-414-229-6958; Tel: +1-414-229-3716*

[b]*Chemical Engineering, Arizona State University, USA*

[c]*Civil, Environmental, and Sustainable Engineering, Arizona State University, USA*

† Electronic supplementary information (ESI) available: Detailed description of the Rietveld refinement of the XRD data, and the investigation of the effect of catalyst mass on the photocatalytic activity. See DOI: 10.1039/c3ta11226h

contrary, other studies suggested that electrons transfer from rutile to anatase.[12,13,22,23] Among them, Hurum *et al.*[12,13] used electron paramagnetic resonance (EPR) spectroscopy to monitor the direction of electron migration; they suggested that electrons transfer from rutile to anatase because the energy levels of the electron trapping sites in anatase are lower than that of the rutile CB. In addition, the interfacial sites between anatase and rutile facilitate the electron transport and prevent the recombination of e^- and h^+.[12,13] However, some recent studies reported that there are no interactions between the two phases in P25, and anatase and rutile independently catalyze reactions.[24]

Analogous to anatase–rutile mixed-phase TiO_2, anatase–brookite heterojunctions are expected to enhance charge separation as well, probably even superior to anatase–rutile. Possible reasons are: (1) our previous study[4] has discovered that brookite itself is more active than rutile in CO_2 photoreduction; (2) the CB edge of brookite is slightly above that of anatase,[25] making it possible for electrons to transfer from brookite to anatase even in the absence of anatase trapping sites. Some experimental evidence exists in the literature indicating that anatase–brookite mixtures are more active than anatase–rutile mixtures (*e.g.* P25)[26] and pure anatase[7,27] for photo-oxidation of organic compounds. While bicrystalline anatase–brookite TiO_2 has demonstrated certain promising photocatalytic oxidation abilities, the relationship between phase composition and catalytic activity is not clear. In the case of anatase and rutile mixtures, there is an optimum phase content (*i.e.*, anatase–rutile = 77/23) that corresponds to the highest photoactivity.[28,29] The optimum phase composition in an anatase–brookite has never been explored; moreover, no studies have been reported on its application in CO_2 photoreduction and the correlation of material properties with photocatalytic activities.

In this work, we have synthesized pure phase anatase, brookite, and mixed-phase anatase–brookite catalysts with a controllable brookite fraction. For the first time in the literature, we have investigated and report the effect of TiO_2 phase fractions and nanostructures on CO_2 photoreduction, including the optimum phase composition for CO_2 photoreduction. We have also conducted *in situ* spectroscopic studies to investigate the CO_2 reduction mechanism.

2 Experiments

2.1 Catalyst preparation

TiO_2 nanocrystals of single-phase anatase and brookite and mixed-phase anatase–brookite were prepared using a hydrothermal method.[19] In a typical preparation process, 10 ml titanium bis(ammonium lactate)dihydroxide (50% in H_2O, Sigma-Aldrich), was mixed with 90 ml urea solution (with varying concentration of urea) and sealed in a 250 ml Teflon-lined autoclave, which was then sealed and placed in an electric oven at 160 °C for 24 h. After the hydrothermal process, the autoclave was naturally cooled down to room temperature. The precipitates were centrifuged, washed with de-ionized water, dried at 60 °C for 12 h, grinded and finally calcined at 400 °C for 3 h. To prepare pure phase anatase, the urea concentration in the precursor solution was 0.1 M. A urea concentration above 0.1 M led to the formation of an anatase–brookite mixture, and the brookite content increased with the urea concentration. At 7.0 M, pure brookite was formed. Table 1 summarizes the relation between the urea concentration and the phase composition. The prepared TiO_2 mixtures were denoted as A_xB_y, where x and y are the phase fraction of anatase and brookite, respectively.

2.2 Catalyst characterization

The crystal structures of the prepared TiO_2 samples were identified by X-ray diffraction (Scintag XDS 2000) using Cu Kα irradiation at 45 kV and a diffracted beam monochromator operated at 40 mA in the 2θ range from 20° to 50° at a scan rate of 2° min^{-1}. The crystallite sizes of catalysts were calculated by the Scherrer equation. Quantitative phase composition analysis of as prepared TiO_2 was performed using Rietveld refinement method by the MAUD software (version 2.33).[30,31] The XRD data of as prepared TiO_2 samples together with the known standard data of anatase (tetragonal) and brookite (orthorhombic) were loaded into the MAUD software. The isotropic model and anisotropic model were chosen for anatase and brookite, respectively.[30] Peak positions and scale factors were adjusted before quantitative analysis.

Raman spectroscopy was carried out with a Renishaw 1000B system in the range of 100–700 cm^{-1}. The specific surface areas of all synthesized catalysts were obtained by nitrogen adsorption–desorption at 77 K using the Brunauer–Emmett–Teller (BET) method (Micrometrics, ASAP 2020). UV-vis spectra of the catalysts were obtained by a diffuse reflectance UV-vis spectrophotometer (Ocean Optics) using $BaSO_4$ as the background. The morphologies of TiO_2 polymorphs were characterized by scanning electron microscopy (SEM, Hitachi S4800), using a secondary electron detector (SE) at an accelerating voltage range of 5–10 kV. Transmission electron microscopy (TEM) and high-resolution transmission electron microscopy (HRTEM) were carried out

Table 1 The characteristics of prepared TiO_2 catalysts including crystal phase content, BET specific surface area, pore size and pore volume, band gap, and the corresponding urea concentration in the precursor solution during material synthesis

Catalyst	Urea conc. (M)	Anatase phase (%)	Brookite phase (%)	BET specific surface area (m^2 g^{-1})	Pore size (nm)	Pore volume (cm^3 g^{-1})	Band gap (eV)
A_{100}	0.1	100	0	145.6	6.2	0.23	3.08
$A_{96}B_4$	0.25	96	4	134.5	5.9	0.20	3.12
$A_{75}B_{25}$	0.5	75	25	140.3	5.5	0.20	3.15
$A_{50}B_{50}$	1.0	50	50	84.5	7.0	0.18	3.15
$A_{37}B_{63}$	1.5	37	63	70.2	10.7	0.19	3.20
B_{100}	7.0	0	100	76.6	18.4	0.35	3.22

with 300 keV electrons in a Hitachi H9000NAR instrument with 0.18 nm point and 0.11 nm lattice resolutions, to obtain crystal structure, morphology, and lattice information of TiO_2 nanocrystals.

2.3 Photocatalytic activity measurement

The photocatalytic reduction of CO_2 over the TiO_2 samples was conducted in a photoreactor operating in a continuous-flow mode. The experimental setup was similar to that described in our previous work.[1] A solar simulator (Oriel, 150 W) was used as the light source. The light intensity was 69.6 mW cm^{-2} for 200 < λ < 1000 nm and 12.5 mW cm^{-2} for 200 < λ < 400 nm (UV region), as measured by a spectroradiometer (International Light Technologies ILT950). The photoreactor was cylindrical shape with a stainless steel housing and a quartz window (dia. = 7.5 cm). For each test, 100 mg TiO_2 powder catalyst was evenly dispersed onto a glass-fiber filter that was placed at the bottom of the photoreactor facing the light source. Ultrahigh purity CO_2 (99.999%, Praxair) regulated by a mass-flow controller (MFC) continuously passed through a bubbler that contained de-ionized water. The resulting gas mixture (CO_2 and 2.3 vol% H_2O vapor) was introduced to the photoreactor. A gas chromatograph (GC, Agilent 7890A) equipped with a thermal conductivity detector (TCD) and a flame ionization detector (FID) was used to continuously analyze the gaseous products. A Carboxen-1010 PLOT capillary column coupled with the TCD was used for CO measurement, and a HP-PLOT-Q capillary column coupled with the FID was used for CH_4 measurement.

2.4 *In situ* DRIFTS analysis

In situ diffuse reflectance infrared Fourier transform spectroscopy (DRIFTS) is one of the most powerful tools to identify and characterize adsorption species and reaction intermediates on the catalyst surface; however, it is not often used in studying CO_2 activation and reduction on TiO_2. In this work, *in situ* DRIFTS analysis was conducted to evaluate the interaction of CO_2 and H_2O vapor with the photocatalyst surface in the dark and under photo-illumination. Detailed description of the DRIFTS setup can be found in our previous publication.[4] The *in situ* experiments were conducted under such a sequential procedure: (1) the catalyst was purged with He at 200 °C to remove the residual water and hydroxyl groups on the surface, (2) a CO_2–H_2O mixture was continuously introduced to the DRIFTS cell for 30 min when the intensities of adsorption peaks of CO_2 and H_2O reached saturation levels, and (3) the light from the solar simulator was introduced to the DRIFTS cell by a liquid guide. The IR spectra were recorded as a function of time to monitor the surface adsorbed species during H_2O and CO_2 adsorption in the dark (step 2) and the surface intermediates during the photocatalytic reaction process (step 3).

3 Results and discussion

3.1 Crystal structure and morphology of TiO_2 polymorphs

The urea concentration in the precursor solution was directly related to the phase content of the prepared TiO_2 nanocrystals (Table 1). The crystal structure of TiO_2 with different ratios of anatase–brookite was confirmed by XRD, as shown in Fig. 1a. The anatase–brookite ratios were calculated by the Rietveld refinement method. Fig. 1b shows the Rietveld refinement result of $A_{50}B_{50}$ as an example. It demonstrates three important aspects about the crystal structure of TiO_2: (1) the peak positions of the fitting curve match the standard anatase and brookite peak positions nicely, which directly proved the bicrystalline TiO_2 was composed of anatase and brookite mixture crystal phases; (2) the black solid fitting curve (from refinement result) and the blue dots (experimental XRD data) match very well, indicating a high goodness of fitting (GOF); and (3) the very small fluctuation of the GOF curve at the bottom indicates a high quality refinement result.[32] The phase ratio is calculated by the MAUD software automatically after the appropriate refinement. The Rietveld refinement results for all the bicrystalline TiO_2 samples are shown in Fig. S1 to S4 in the ESI.†

At the lowest concentration of urea (0.1 M), pure phase anatase (JCPDS no. 21-1272), *i.e.*, A_{100}, was obtained. With an increasing concentration of urea up to 1.5 M, bicrystalline anatase–brookite mixtures with an increasing brookite fraction, *i.e.*, $A_{96}B_4$, $A_{75}B_{25}$, $A_{50}B_{50}$, and $A_{37}B_{63}$ were formed. At the highest urea concentration (7.0 M), pure brookite (JCPDS no. 29-1360) was obtained. The existence of brookite in the resultant powders is readily discernible from its unique (121),

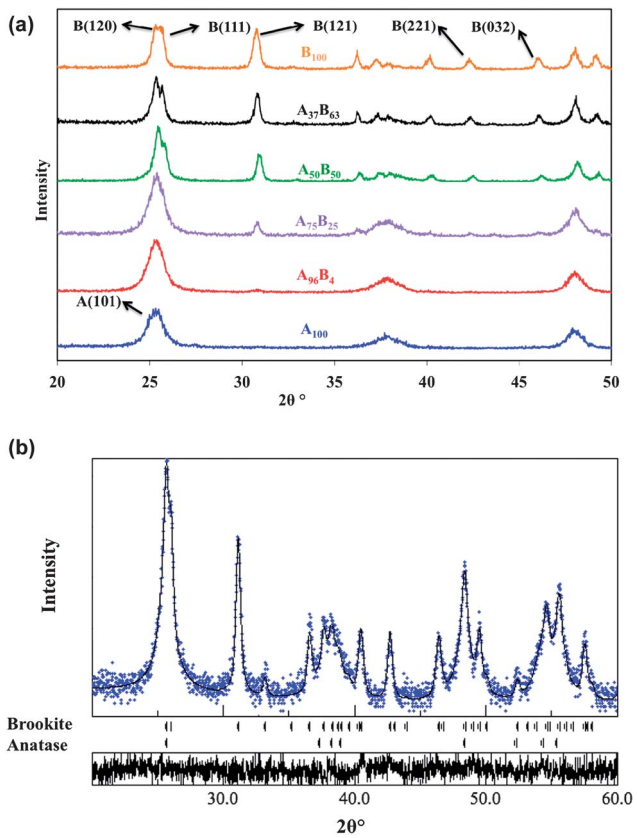

Fig. 1 XRD patterns of the prepared TiO_2 catalyst powders with different fractions of anatase and brookite phases (a); Rietveld refinement result for the $A_{50}B_{50}$ sample – solid line: fitting curve; blue dots: experimental data; bottom panel: goodness of fitting (GOF) (b).

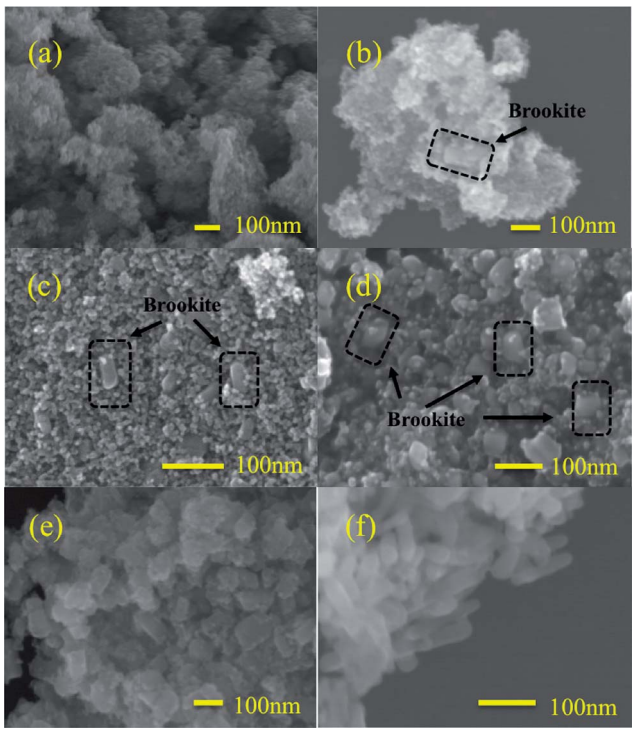

Fig. 2 SEM images of A_{100} (a), $A_{96}B_4$ (b), $A_{75}B_{25}$ (c), $A_{50}B_{50}$ (d), $A_{37}B_{63}$ (e), and B_{100} (f). The circled areas in black in (b), (c), and (d) indicate brookite nanobricks.

(221), and (032) diffraction peaks at 30.81, 42.34, 46.07° (2θ), respectively (Fig. 1a). Clearly, through adjusting the concentration of urea, anatase, brookite or mixtures with controllable anatase–brookite phase fractions were successfully prepared.

The morphologies of the prepared TiO_2 nanocrystals were examined by SEM, as shown in Fig. 2. Pure anatase, A_{100}, consisted of agglomerate sphere-shaped nanoparticles, while pure brookite, B_{100}, was rod-shaped nanoparticles. For anatase–brookite mixtures, the brookite nanorods appeared to have a lower aspect ratio (brick-shaped) than those observed in pure brookite (rod-shaped). With an increasing brookite fraction in the anatase–brookite mixtures, the number of nanobricks/nanorods increased and the size became larger. Eventually, the brookite crystals evolved from nanobricks to nanorods as the brookite content approached 100%.

The particle size, morphology, and lattice structure of $A_{75}B_{25}$ were further evaluated by TEM and HRTEM, as shown in Fig. 3. Mixtures of spherical and rod-shaped nanoparticles were observed (Fig. 3a). The spherical particles are in the range of 5–10 nm and the nanorod has a width of 20 nm and length of 60 nm. HRTEM images in Fig. 3b and c clearly demonstrated that the spherical nanoparticle was anatase (lattice spacing = 0.35 nm, corresponding to the (101) plane) and the nanorod was brookite (lattice spacing = 0.91, 0.35 nm, corresponding to (100) and (210) plane, respectively).[4]

Fig. 3b and c also demonstrated the overlapping anatase and brookite particles and the interface between them. In Fig. 3b the lattice fringe becomes fuzzy and even discontinued (Region 1) where the anatase and brookite crystals overlap. An anatase particle was also located at the edge of brookite (Region 2). Besides those simple attachments of anatase particles to brookite particles, a coherent interface between anatase and brookite could be formed. As shown in Fig. 3c, the lattice spacing of the anatase (101) plane matches that of the brookite (210) plane (0.35 nm) in the region where the two particles overlap (Region 3). This observation agrees with theoretical simulation results that the brookite (210) surface and the most stable anatase (101) plane have the same type of building block, and both phases may share a common boundary.[33] On anatase (101) all the octahedron units are closely packed, while on brookite (210) the rotated units are closely packed only along the direction.[33,34] This difference may cause a distortion at the interface between the two crystal phases. The HRTEM images in Fig. 3 demonstrated that when anatase and brookite nanocrystals grow in the same orientation, a unique interface between them could be possibly formed.

Raman spectra (Fig. 4) have further proved the existence of both anatase and brookite crystals in the A–B mixture ($A_{75}B_{25}$). Brookite has the most intense Raman bands at ~245, ~320, ~399, ~410, and ~637 cm^{-1}, while anatase has intense Raman bands at ~399, ~519, and ~639 cm^{-1}.[35] As compared with the spectra of A_{100} and B_{100}, the Raman spectrum of $A_{75}B_{25}$ included all the bands of the two crystal phases, thus indicating a mixed phase of anatase and brookite.

3.2 Textural and optical properties of TiO_2 polymorphs

Fig. 5 shows that the N_2 adsorption–desorption isotherms for all the six TiO_2 samples are Type IV, characteristics of materials with mesoporous structures. The isotherms of B_{100} and $A_{37}B_{63}$ have a similar shape and close at a higher relative pressure

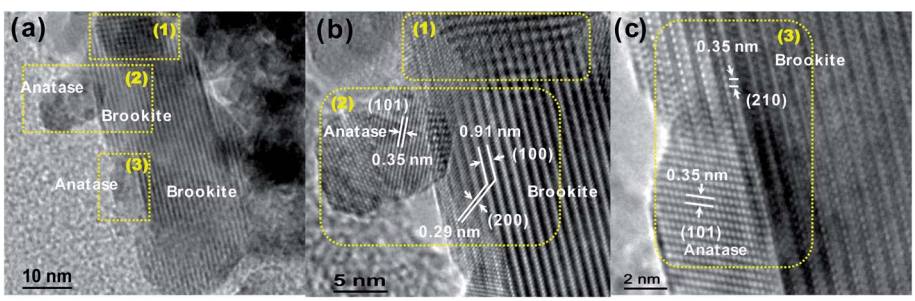

Fig. 3 TEM images of $A_{75}B_{25}$ (a), and HRTEM images of $A_{75}B_{25}$ (b and c).

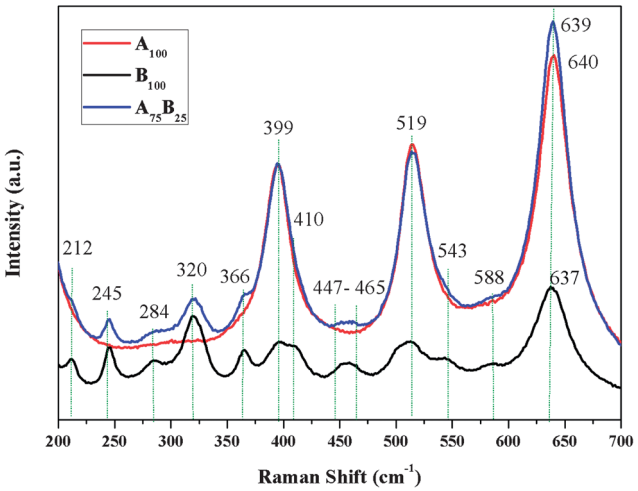

Fig. 4 Raman spectra of A_{100}, B_{100}, and $A_{75}B_{25}$ samples.

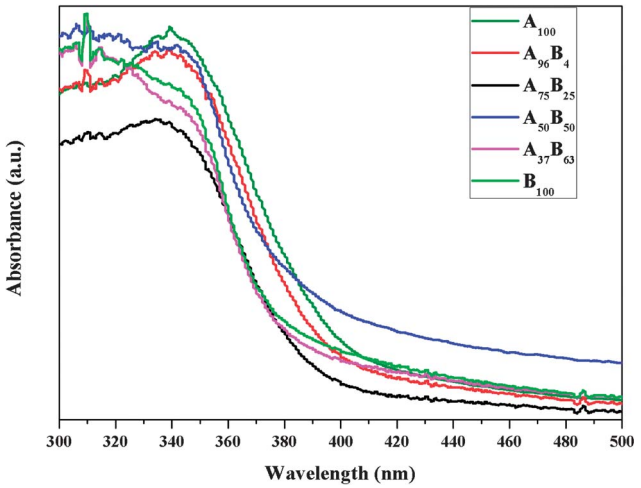

Fig. 6 The UV-vis diffuse reflectance spectra (displayed in absorbance) of the prepared TiO_2 catalysts.

compared to those of A_{100}, $A_{96}B_4$, $A_{75}B_{25}$, and $A_{50}B_{50}$. Correspondingly, the calculated pore sizes of anatase-rich TiO_2 are smaller than those of brookite-rich TiO_2 (Table 1). This is because the inter-particle spaces between the agglomerated anatase TiO_2 nanoparticles were smaller than those between the nanobricks/nanorods in brookite-rich TiO_2. Table 1 also compared the BET specific surface areas of the various TiO_2 catalysts. The surface areas of anatase and anatase-rich samples (A_{100}, $A_{96}B_4$, and $A_{75}B_{25}$) were close (around 140 m^2 g^{-1}) and were twice as much as those of brookite-rich and pure brookite TiO_2 ($A_{37}B_{63}$ and B_{100}). The sharp decrease in surface area from $A_{75}B_{25}$ to $A_{50}B_{50}$ can be explained from their SEM images in Fig. 2: for $A_{75}B_{25}$, brookite nanobricks are embedded in agglomerated anatase nanoparticles; whereas, for $A_{50}B_{50}$, a smaller amount of anatase nanoparticles are dispersed on the surfaces of brookite nanobricks. The surface area of the larger brookite crystals is smaller than that of the smaller anatase crystals.

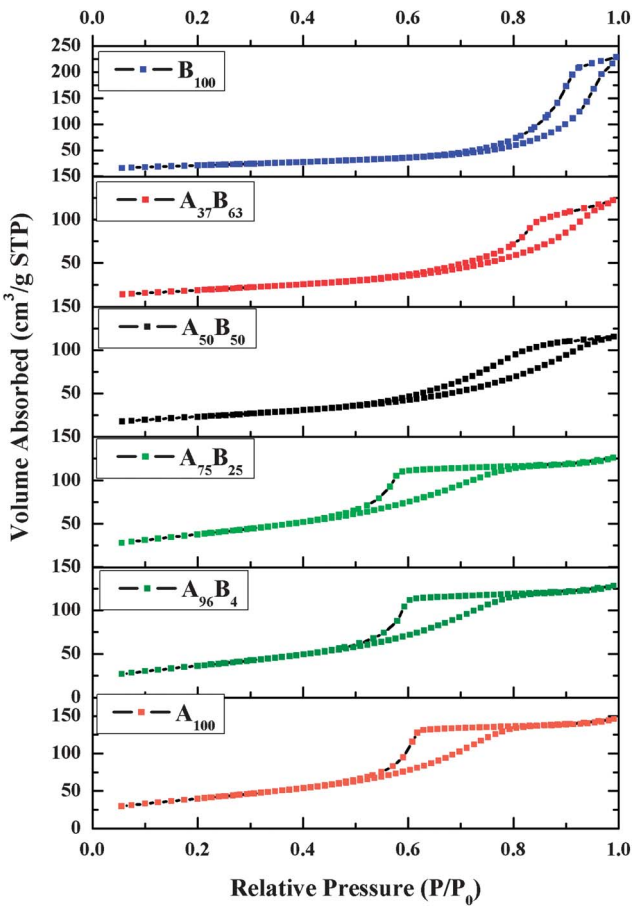

Fig. 5 Nitrogen adsorption–desorption isotherms for the prepared TiO_2 catalysts.

Fig. 6 compares the UV-vis spectra, displayed in absorbance units, of the prepared TiO_2 catalysts. The absorption edge of A_{100} is around 402 nm, corresponding to a band gap at 3.08 eV, close to the value reported in the literature.[4,36] An increase in the brookite fraction in the anatase–brookite mixture results in a blue shift in the absorption spectra and an increase in the band gap (listed in Table 1). B_{100} has the largest band gap at 3.22 eV. The observed larger band gap of brookite than anatase agrees with that reported in the literature,[19] as the conduction band of brookite is positioned at 0.14 eV more negative than that of anatase.[37] The catalysts after CO_2 photoreduction experiments were also characterized by UV-vis, and no changes in the catalyst band gap were observed.

3.3 Photocatalytic activity for CO_2 reduction

The photocatalytic activities of the prepared TiO_2 catalysts were tested for CO_2 photoreduction with H_2O vapor. Background experiments were first conducted under the following conditions: (1) blank glass-fiber filter in the reactor without loading catalysts under the irradiation of solar simulator in a CO_2 + H_2O flow; (2) catalysts loaded on a glass-fiber filter in the dark in a CO_2 + H_2O flow; and (3) catalysts loaded on a glass-fiber filter under simulated solar radiation in a He + H_2O flow. In all cases, no carbon-containing products were detected. These

background tests indicated that any carbon-containing products formed (described in the subsequent part of this paper) were generated solely from the reaction of CO_2 + H_2O over the photocatalysts under light irradiation, not from any surface impurities on the catalysts.

As consistent with our previous studies,[4,5] CO was the major product and CH_4 was the minor product formed during CO_2 photoreduction with H_2O vapor, and no other products (such as H_2) were detected. The absence of H_2 production was consistent with the literature that H_2 production is prominent only in the presence of noble metal co-catalysts (*e.g.*, Pt, Ag)[1,38] or in the presence of sacrificial agents (*e.g.*, CH_3OH).[1,39] CH_4 production was much lower than CO production, likely because the formation of CH_4 requires the complete reduction of CO_2 to C, and a subsequent reaction with available H atoms from the decomposition of water vapor on the same catalyst surface. If the CO desorbs from the surface before it can be fully reduced, then the formation of CH_4 is impacted.

Fig. 7 compares the production rates of CO on various TiO_2 catalysts. For each test 100 mg of catalyst was used (see Fig. S5 in the ESI† regarding the additional experiments using different amount of catalysts and the justification of using 100 mg to study the intrinsic catalyst activity). The test for each sample was repeated twice (a fresh catalyst was used each time), and the errors were within reasonable experimental uncertainties. The CH_4 production rates are not plotted in Fig. 7 because they were too low (less than 0.005 μmol h^{-1}) and did not vary significantly for different catalysts. B_{100} had the lowest activity among all the catalysts, with a CO production rate at 0.07 μmol h^{-1}. A_{100} had a CO production rate at 0.12 μmol h^{-1}, higher than that of B_{100}. The bicrystalline samples with dominating anatase phase ($A_{96}B_4$ and $A_{75}B_{25}$) or equal anatase–brookite content ($A_{50}B_{50}$) were the most active ones, having a CO production rate from 0.16 to 0.21 μmol h^{-1}. The activity of $A_{75}B_{25}$ was nearly twice as high as that of A_{100} and three times as high as that of B_{100}. Further increasing the brookite content (*i.e.*, brookite-rich $A_{37}B_{63}$) led to a lower CO production rate at 0.12 μmol h^{-1}.

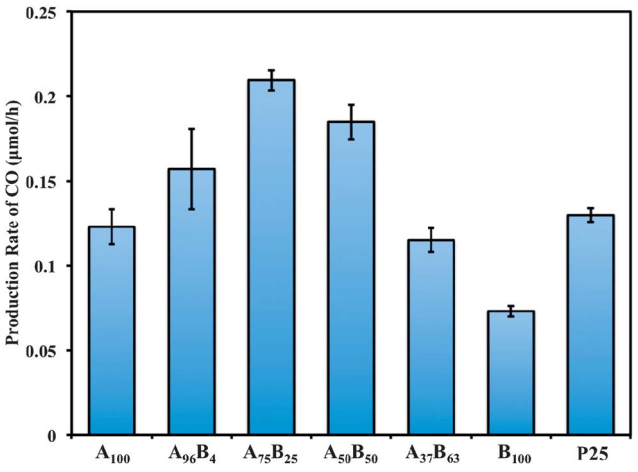

Fig. 7 The production rates of CO using various TiO_2 catalysts (the reactants were a gas mixture of 97.7 vol% CO_2 and 2.3 vol% H_2O; 100 mg catalysts were used for each test).

Commercial TiO_2 P25 was also tested as comparison; it had a CO production rate of 0.13 μmol h^{-1}, lower than the anatase-rich bicrystalline anatase–brookite samples. The above results demonstrate that the anatase-rich bicrystalline anatase–brookite mixtures are superior to single crystalline anatase or brookite and anatase–rutile mixtures (*i.e.*, P25). Considering that pure anatase A_{100} had the largest specific surface area and the smallest band gap (Table 1), the higher activity of bicrystalline anatase–brookite is very likely ascribed to the interactions between the anatase and brookite nanocrystals. This interaction between anatase and brookite seems to be more effective than that between anatase and rutile (as in P25). In addition, it is reasonable to find that anatase-rich A–B mixtures are more active than brookite-rich A–B mixtures since pure anatase is more active than pure brookite.

The experimental results in Fig. 7 indicate that anatase rich A–B mixture with 75% anatase and 25% brookite, *i.e.*, $A_{75}B_{25}$ is the most active among all the prepared catalysts. There are three possible reasons for its superior activity: (1) the more negative CB band of brookite may induce electron transfer from brookite to anatase, thus enhancing charge separation; (2) the facilitated formation of the intrinsic defect sites in brookite may enhance electron trapping,[40] and (3) the distorted interfaces between anatase and brookite crystals (as evidenced in the HRTEM images) may facilitate interfacial electron transport and prevent the recombination of electron–hole pairs.[41] It is also noticed from Fig. 6 that anatase-rich A–B mixtures such as $A_{75}B_{25}$ showed less light absorption in the UV region compared to other samples; the highest photocatalytic activity of $A_{75}B_{25}$ implies the importance of interfacial charge transfer between the A and B nanocrystals.

Additional experiments were conducted to explore the potential O_2 production from H_2O oxidation using the sample of $A_{75}B_{25}$. Prior to the photocatalytic reaction, the photoreactor was purged with a CO_2–H_2O gas mixture to eliminate the air inside the reactor. However, even after purging for a few hours, there was still background O_2 (in a few hundred ppm range) together with N_2 detected in the reactor effluent gas. Hence, a better indicator of O_2 production by the catalyst is the volumetric ratio of O_2/N_2 in the effluent gas, as also suggested in the literature and in our previous work.[4,42] Fig. 8 shows the O_2/N_2 ratio before, during and after the photoreaction, when the reactor effluent gas was sampled every 15 min. Before turning on the light (in the dark), the O_2/N_2 ratio was steady. Immediately upon photo-illumination, the O_2/N_2 ratio dramatically decreased in the first 60 min and then gradually increased. The sharp decrease is probably due to the consumption of residual O_2 in the reactor through the reaction with photogenerated electrons $O_2 + e^- \rightarrow O_2^-$ and consecutive reactions.[4] In the meantime upon photo-illumination, the production of CO and CH_4 occurred, and the rates increased to their maximum in 30 to 60 min (see Fig. S6, ESI†). This indicates that although O_2 competes with CO_2 for photogenerated electrons, it cannot completely block the electron transfer to CO_2, since the concentration of CO_2 was several orders of magnitude higher than O_2 in the reactor. The gradual increase in the O_2/N_2 ratio after 60 min photo-irradiation (Fig. 8) indicates the generation of O_2 through oxidation of H_2O with photogenerated holes, $H_2O + 2h^+ \rightarrow 2H^+ +$

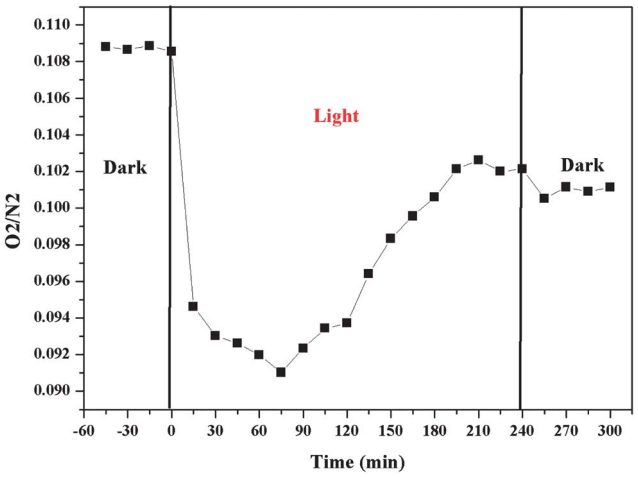

Fig. 8 Time dependence of the volumetric ratio of O_2/N_2 before, during and after the photoreduction of CO_2 with H_2O on the $A_{75}B_{25}$.

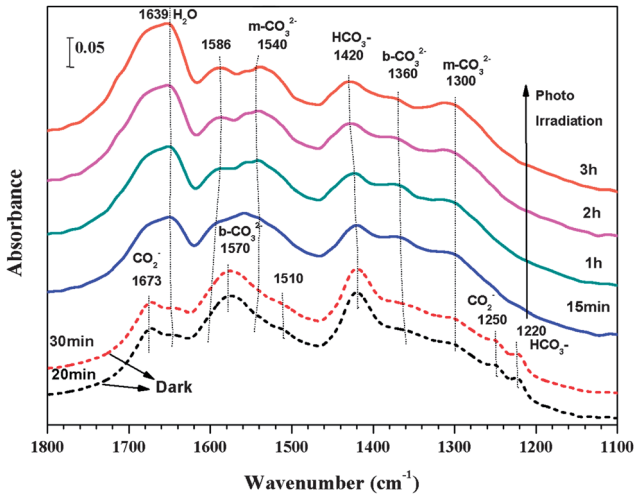

Fig. 9 *In situ* DRIFTS spectra of CO_2 and H_2O adsorption on $A_{75}B_{25}$ for 30 min in the dark (short-dash lines), and subsequent photoreduction process under the UV-vis light irradiation for 3 h (solid lines).

$(1/2)O_2$. Because the increasing amount of generated O_2 overweighed the concurrent O_2 consumption process, the net result was that the O_2/N_2 ratio gradually increased with time and finally reached in a steady state after 200 min. After turning off the light (the second dark period), the O_2/N_2 ratio dropped slightly. This result again verified the generation of O_2 during the photocatalytic CO_2 reduction with H_2O vapor.

3.4 *In situ* DRIFTS investigation on surface chemistry and reaction intermediates

The lifetime of the catalysts used in this work was about 4 h, as the production rate of CO dropped to a very low level after 4 h of photo-illumination (results not shown). The short lifetime of photocatalysts (typically in the range of a few hours, if without sacrificial agents like methanol) is a well known research challenge in photoreduction applications including H_2 production from water or CO_2 reduction. The *in situ* DRIFTS analysis in this work is helpful to explore the surface chemistry and the reason for catalyst deactivation.

As shown in Fig. 9, in the dark, CO_2–H_2O adsorption on $A_{75}B_{25}$ resulted in the formation of bicarbonate (HCO_3^-, 1220 and 1420 cm^{-1}), bidentate carbonate (b-CO_3^{2-}, 1360 and 1570 cm^{-1}), monodentate carbonate (m-CO_3^{2-}, 1300 and 1540 cm^{-1}), and carboxylate (CO_2^-, 1250 and 1673 cm^{-1}).[4,43,44] The intensities of the peaks remained almost unchanged from 20 min to 30 min, indicating that the adsorption of CO_2–H_2O reached the saturated level on the surface of $A_{75}B_{25}$. Immediately upon photo-irradiation for 15 min, the peaks for HCO_3^- and CO_2^- species decreased or even disappeared, while the peak for surface H_2O (1639 cm^{-1})[4] and CO_3^{2-} increased. Upon increasing the photo-illumination time from 15 min to 3 h, the intensities of the H_2O and CO_3^{2-} peaks gradually increased, while that of HCO_3^- was gradually decreased and CO_2^- completely disappeared.

In our previous studies,[45] we found that HCO_3^- and CO_2^-, formed from CO_2 interaction with OH groups and Ti^{3+} sites, are the possible intermediates for CO_2 photoreduction to CO and C_1 fuels (*e.g.*, CH_4) once the dissociative H atom is available. The DRIFTS results in Fig. 9 again demonstrated the importance of the HCO_3^- and CO_2^- as the CO_2 reduction intermediates, evidenced by the weakened HCO_3^- peak and the disappearance of CO_2^- upon photo-illumination. The increase of CO_3^{2-} species could partially result from HCO_3^- transformation. The increase in surface H_2O may be explained as follows. It is known that H_2O and CO_2 competitively adsorb on TiO_2. H_2O and CO_2 adsorption reached equilibrium in the dark. Upon photo-illumination, this equilibrium was broken when adsorbed CO_2 species was reduced to CO and desorbed into the gas phase. Hence, some surface sites like OH groups became available for incoming gas molecule adsorption. Because H_2O has a higher binding energy with surface OH groups than CO_2, once the OH groups were re-exposed, most of them may be occupied by H_2O, and thus preventing subsequent CO_2 adsorption on the surface. The lack of continuous formation of active CO_2 adsorption species (HCO_3^- and CO_2^-, not CO_3^{2-}) species may cause the observed catalyst deactivation over a few hours observed in the photocatalytic activity measurements. The above described DRIFTS results have provided significant insights into the reaction mechanism and catalyst deactivation, which have been rarely studied in the literature.

4 Conclusions

For the first time in the literature, this paper reports the superior activity of anatase-rich anatase–brookite mixtures for the photocatalytic reduction of CO_2 to fuels. The interfaces between anatase and brookite nanocrystals are believed to enhance photo-induced charge transfer and electron–hole separation, and thus they are more active than single-phase anatase or brookite. Anatase-rich A–B mixtures are more active than brookite-rich A–B mixtures since the anatase nanoparticles used in this study have higher specific surface area and smaller band gaps than the brookite nanorods that were used. The anatase-rich A–B mixture ($A_{75}B_{25}$) was far more active than the

anatase-rich A–R mixture with similar anatase fraction (*i.e.* P25). This important finding suggests a new direction for the development of efficient catalysts for CO_2 photoreduction to fuels, *i.e.* brookite-containing mixed phase TiO_2 nanocrystals including tri-phasic TiO_2 (anatase–brookite–rutile). Our *in situ* DRIFTS analysis has demonstrated that HCO_3^- and CO_2^- species are important reaction intermediates for CO production. Unfortunately, the formation of those species cannot be sustained which may lead to the deactivation of the photocatalysts. Continued research in advancing the understanding of the surface chemistry is important to the design of more efficient photocatalyst in CO_2 reduction.

Acknowledgements

This work was supported by National Science Foundation (CBET-1067233 and CBET-1067340).

Notes and references

1 C. Y. Zhao, A. Krall, H. L. Zhao, Q. Y. Zhang and Y. Li, *Int. J. Hydrogen Energy*, 2012, **37**, 9967–9976.
2 Y. Izumi, *Coord. Chem. Rev.*, 2013, **257**, 171–186.
3 A. Dhakshinamoorthy, S. Navalon, A. Corma and H. Garcia, *Energy Environ. Sci.*, 2012, **5**, 9217–9233.
4 L. J. Liu, H. L. Zhao, J. M. Andino and Y. Li, *ACS Catal.*, 2012, **2**, 1817–1828.
5 Q. Y. Zhang, Y. Li, E. A. Ackerman, M. Gajdardziska-Josifovska and H. L. Li, *Appl. Catal., A*, 2011, **400**, 195–202.
6 Y. L. Liao, W. X. Que, Q. Y. Jia, Y. C. He, J. Zhang and P. Zhong, *J. Mater. Chem.*, 2012, **22**, 7937–7944.
7 T. Ozawa, M. Iwasaki, H. Tada, T. Akita, K. Tanaka and S. Ito, *J. Colloid Interface Sci.*, 2005, **281**, 510–513.
8 D. Reyes-Coronado, G. Rodriguez-Gattorno, M. E. Espinosa-Pesqueira, C. Cab, R. de Coss and G. Oskam, *Nanotechnology*, 2008, **19**, 145605.
9 M. Landmann, E. Rauls and W. G. Schmidt, *J. Phys.: Condens. Matter*, 2012, **24**, 195503.
10 G. Liu, X. W. Wang, Z. G. Chen, H. M. Cheng and G. Q. Lu, *J. Colloid Interface Sci.*, 2009, **329**, 331–338.
11 J. T. Carneiro, T. J. Savenije, J. A. Moulijn and G. Mul, *J. Phys. Chem. C*, 2011, **115**, 2211–2217.
12 D. C. Hurum, A. G. Agrios, S. E. Crist, K. A. Gray, T. Rajh and M. C. Thurnauer, *J. Electron Spectrosc. Relat. Phenom.*, 2006, **150**, 155–163.
13 D. C. Hurum, A. G. Agrios, K. A. Gray, T. Rajh and M. C. Thurnauer, *J. Phys. Chem. B*, 2003, **107**, 4545–4549.
14 Q. Zhu, J. S. Qian, H. Pan, L. Tu and X. F. Zhou, *Nanotechnology*, 2011, **22**, 395703.
15 V. Stengl and D. Kralova, *Mater. Chem. Phys.*, 2011, **129**, 794–801.
16 Q. X. Deng, M. D. Wei, Z. S. Hong, X. K. Ding, L. L. Jiang and K. M. Wei, *Curr. Nanosci.*, 2010, **6**, 479–482.
17 D. Dambournet, I. Belharouak and K. Amine, *Chem. Mater.*, 2010, **22**, 1173–1179.
18 A. Garcia-Ruiz, A. Morales and X. Bokhimi, *J. Alloys Compd.*, 2010, **495**, 583–587.
19 T. A. Kandiel, A. Feldhoff, L. Robben, R. Dillert and D. W. Bahnemann, *Chem. Mater.*, 2010, **22**, 2050–2060.
20 H. Pan, X. F. Qiu, I. N. Ivanovc, H. M. Meyer, W. Wang, W. G. Zhu, M. P. Paranthaman, Z. Y. Zhang, G. Eres and B. H. Gu, *Appl. Catal., B*, 2009, **93**, 90–95.
21 T. Kawahara, Y. Konishi, H. Tada, N. Tohge, J. Nishii and S. Ito, *Angew. Chem., Int. Ed.*, 2002, **41**, 2811–2813.
22 G. Liu, X. X. Yan, Z. G. Chen, X. W. Wang, L. Z. Wang, G. Q. Lu and H. M. Cheng, *J. Mater. Chem.*, 2009, **19**, 6590–6596.
23 G. H. Li, C. P. Richter, R. L. Milot, L. Cai, C. A. Schmuttenmaer, R. H. Crabtree, G. W. Brudvig and V. S. Batista, *Dalton Trans.*, 2009, 10078–10085.
24 B. Ohtani, O. O. Prieto-Mahaney, D. Li and R. Abe, *J. Photochem. Photobiol., A*, 2010, **216**, 179–182.
25 A. Di Paola, M. Bellardita, R. Ceccato, L. Palmisano and F. Parrino, *J. Phys. Chem. C*, 2009, **113**, 15166–15174.
26 J. C. Yu, L. Z. Zhang and J. G. Yu, *Chem. Mater.*, 2002, **14**, 4647–4653.
27 S. Ardizzone, C. L. Bianchi, G. Cappelletti, S. Gialanella, C. Pirola and V. Ragaini, *J. Phys. Chem. C*, 2007, **111**, 13222–13231.
28 S. Bakardjieva, J. Subrt, V. Stengl, M. J. Dianez and M. J. Sayagues, *Appl. Catal., B*, 2005, **58**, 193–202.
29 M. Boehme and W. Ensinger, *Nano-Micro Lett.*, 2011, **3**, 236–241.
30 H. R. Wenk, L. Lutterotti and S. C. Vogel, *Powder Diffr.*, 2010, **25**, 283–296.
31 M. Rezaee, S. M. M. Khoie and K. H. Liu, *CrystEngComm*, 2011, **13**, 5055–5061.
32 B. H. Toby, *Powder Diffr.*, 2006, **21**, 67–70.
33 X. Q. Gong and A. Selloni, *Phys. Rev. B: Condens. Matter Mater. Phys.*, 2007, **76**, 11.
34 Rashmi, N. Singh and A. K. Sarkar, *Powder Diffr.*, 2004, **19**, 141–144.
35 K. R. Moonoosawmy, H. Katzke, M. Es-Souni, M. Dietze and M. Es-Souni, *Langmuir*, 2012, **28**, 6706–6713.
36 K. Nagaveni, M. S. Hegde, N. Ravishankar, G. N. Subbanna and G. Madras, *Langmuir*, 2004, **20**, 2900–2907.
37 T. A. Kandiel, L. Robben, A. Alkaim and D. Bahnemann, *Photochem. Photobiol. Sci.*, 2013, **12**, 602–609.
38 O. K. Varghese, M. Paulose, T. J. LaTempa and C. A. Grimes, *Nano Lett.*, 2009, **9**, 731–737.
39 X. B. Chen, L. Liu, P. Y. Yu and S. S. Mao, *Science*, 2011, **331**, 746–750.
40 H. Pan, B. Gu and Z. Zhang, *J. Chem. Theory Comput.*, 2009, **5**, 3074–3078.
41 S. A. Wohlgemuth, R. J. White, M. G. Willinger, M. M. Titirici and M. Antonietti, *Green Chem.*, 2012, **14**, 1515–1523.
42 W.-N. Wang, W.-J. An, B. Ramalingam, S. Mukherjee, D. M. Niedzwiedzki, S. Gangopadhyay and P. Biswas, *J. Am. Chem. Soc.*, 2012, **134**, 11276–11281.
43 W. Su, J. Zhang, Z. Feng, T. Chen, P. Ying and C. Li, *J. Phys. Chem. C*, 2008, **112**, 7710–7716.
44 C.-C. Yang, Y.-H. Yu, B. van der Linden, J. C. S. Wu and G. Mul, *J. Am. Chem. Soc.*, 2010, **132**, 8398–8406.
45 L. J. Liu, C. Y. Zhao and Y. Li, *J. Phys. Chem. C*, 2012, **116**, 7904–7912.

